

Simultaneous reconstruction of quantum process and noise via corrupted sensing

Mengru Ma and Jiangwei Shang*

Key Laboratory of Advanced Optoelectronic Quantum Architecture and Measurement (MOE),
School of Physics, Beijing Institute of Technology, Beijing 100081, China

(Dated: February 6, 2026)

Quantum processes, including quantum gates and channels, are integral to various quantum information tasks, making the efficient characterization of these processes and their underlying noise critically important. Here, we propose a framework for quantum process tomography in the presence of corrupted noise that is able to simultaneously reconstruct the process and corrupted noise. Firstly, within the Choi-state representation, we derive the corresponding generalized restricted isometry property and demonstrate the simultaneous reconstruction of various quantum gates under sparse noise. Moreover, in comparison with the Choi-state scheme, the process-matrix representation is employed to simultaneously reconstruct sparse noise and a broader range of target quantum gates. Our results demonstrate that significant reduction in experimental configurations is achievable even under corrupted noise.

I. INTRODUCTION

The characterization of quantum gates and channels are usually carried out by the fundamental tool of quantum process tomography (QPT), which plays a central role in quantum information processing and quantum error correction [1–7]. However, standard QPT scales poorly: reconstructing a general d -dimensional process requires $O(d^4)$ measurement configurations and parameters, which becomes prohibitive even for moderate system sizes. Consequently, to mitigate the problem of exponential scaling of QPT resources, a number of alternative methods have been developed for efficient and selective estimation of quantum processes [8–10], such as randomized benchmarking [11–13] and Monte Carlo process certification [14–16]. These protocols estimate the average gate fidelity rather than reconstruct the process matrices. In particular, the protocols inspired by compressed sensing (CS) techniques [17, 18] have been applied to QPT, which can dramatically reduce the required number of configurations.

If the process matrix is (nearly) sparse in a known basis (e.g., the Pauli bases), it can be efficiently estimated by minimizing its ℓ_1 -norm [19]. While the process \mathcal{E} was recovered in Ref. [20] by learning the expectation values of its Jamiołkowski state $\rho_{\mathcal{E}}$ without using an ancilla. It is claimed that $O(rd^2 \log d)$ settings were able to characterize \mathcal{E} , where r is the rank of $\rho_{\mathcal{E}}$ (note that \mathcal{E} has Kraus rank r). Reference [21] studied quantum process tomography given the prior information that the process is a unitary or close to a unitary map, reducing the required data needed for high-fidelity estimation. Moreover, Ref. [22] applied compressed sensing techniques to superconducting qubit systems, showing that the number of experimental configurations for a three-qubit Toffoli gate can be reduced by a factor of ~ 40 as compared to standard QPT. These advances collectively

highlight the potential of structured QPT methods in order to enable scalable quantum characterization.

Beyond the latent structure of the process \mathcal{E} such as sparsity or low Kraus rank [23], alternatively, other structural assumptions have also been explored to improve the reconstruction performance. Matrix product states/operators tomography, exploiting low entanglement structure of the states, enables compact and efficient representations [24–27]. For example, tomography schemes that use only a linear number of experimental operations, together with post-processing that scales polynomially with the system size, are particularly effective for states well approximated by matrix product states [24]. Similarly, process tomography techniques based on a locally-purified density operator take advantage of the small bond dimension to characterize the quantum hardware operating circuits of sufficiently low depth [28]. Meanwhile, Bayesian and machine learning-inspired approaches incorporate geometric priors, such as manifold constraints, to learn quantum processes directly from noisy data. These techniques offer flexible, data-driven alternatives that is able to adapt to varying experimental conditions.

Despite these developments, practical implementations of QPT often overlook the impact of corrupted noise in the measurement outcomes. In realistic experiments, occasional measurement errors, detector imperfections, or calibration drifts introduce sparse but potentially corruptions that are not well captured by conventional noise models. Recently, the corrupted sensing quantum state tomography (CSQST) framework was proposed to enable the simultaneous recovery of quantum states and sparse corruption [29]. This naturally motivates extending the simultaneous tomography of quantum states to the characterization of quantum processes, enabling the reconstruction of both the process and the underlying noise.

This work is organized as follows. In Sec. II, we present the corrupted sensing QPT framework via Choi state and derive the associated generalized restricted isometry property. While Sec. III introduces

* jiangwei.shang@bit.edu.cn

the process-matrix scheme for a comparative numerical analysis. Finally, Sec. IV concludes with a summary and outlook for future work.

II. CORRUPTED SENSING QUANTUM PROCESS TOMOGRAPHY VIA CHOI STATE

We first review the restricted isometry property (RIP), from which the generalized RIP, termed GRIP, will be introduced. The linear map $\mathcal{A}(\cdot)$ is said to have RIP with a restricted isometric constant $\delta \in [0, 1]$ if it has the following property [30]:

$$(1 - \delta)\|X\|_F^2 \leq \|\mathcal{A}(X)\|_2^2 \leq (1 + \delta)\|X\|_F^2. \quad (1)$$

Note that for a vector \mathbf{x} , $\|\mathbf{x}\|_2 = (\sum_i |x_i|^2)^{1/2}$ denotes the ℓ_2 -norm, $\|\mathbf{x}\|_1 = \sum_i |x_i|$ is the ℓ_1 -norm, and $\|\mathbf{x}\|_0$ gives the number of non-zero components of \mathbf{x} . For a matrix X , $\|X\|_F = (\sum_i \sigma_i(X)^2)^{1/2}$ represents its Frobenius norm, with $\sigma_i(X)$ being the singular values of X . The rank of $X \in \mathbb{C}^{d \times d}$ is at most r . Alternatively, the restricted isometry constant of \mathcal{A} can be written as

$$\delta_r = \sup_{X \in \mathcal{D}_r} \left| \|\mathcal{A}(X)\|_2^2 - \|X\|_F^2 \right|, \quad (2)$$

where $\mathcal{D}_r = \{X \in \mathbb{C}^{d \times d} : \text{rank}(X) \leq r, \|X\|_F^2 \leq 1\}$, and δ_r is the smallest value of δ .

Definition 1. For the extended matrix $\mathcal{M} = [\mathcal{A}, I] \in \mathbb{C}^{m \times (d+m)}$, it has the GRIP with constant $\delta_{r,s}$ if $\delta_{r,s}$ is the smallest value of δ such that

$$\begin{aligned} (1 - \delta)(\|X\|_F^2 + \|\mathbf{v}\|_2^2) &\leq \left\| \mathcal{M} \begin{bmatrix} X \\ \mathbf{v} \end{bmatrix} \right\|_2^2 \\ &\leq (1 + \delta)(\|X\|_F^2 + \|\mathbf{v}\|_2^2) \end{aligned} \quad (3)$$

holds for the matrix $X \in \mathbb{C}^{d \times d}$ with rank at most r and $\mathbf{v} \in \mathbb{R}^m$ with sparsity $\|\mathbf{v}\|_0 \leq s$.

Note that the sensing matrix \mathcal{A} satisfying the RIP does not necessarily imply that the associated matrix \mathcal{M} would satisfy the GRIP [31].

A. GRIP for corrupted sensing QPT

The GRIP condition for corrupted sensing quantum state tomography is given in Appendix A. Here, considering the Choi-Jamiołkowski isomorphism [32, 33], the process $\mathcal{E}: \mathbb{C}^{d \times d} \rightarrow \mathbb{C}^{d \times d}$ is completely and uniquely characterized by the state

$$\rho_{\mathcal{E}} = (\mathcal{E} \otimes \mathcal{I})(|\Psi\rangle\langle\Psi|), \quad (4)$$

where $|\Psi\rangle = \frac{1}{\sqrt{d}} \sum_{j=0}^{d-1} |j\rangle \otimes |j\rangle$. The state $\rho_{\mathcal{E}} \in \mathbb{C}^{d^2 \times d^2}$ is assumed to satisfy $\text{Tr}(\rho_{\mathcal{E}}) = 1, \rho_{\mathcal{E}} \succeq 0$, and has rank at most r .

Let P^S and P^A be the n -qubit Pauli operators acting on the system and ancilla, respectively. And $P^S, P^A \in \mathbb{C}^{d \times d}$, where $d = 2^n$. We define the Pauli observable as

$$\mathcal{W} = P^S \otimes P^A \in \mathbb{C}^{d^2 \times d^2}, \quad (5)$$

which acts on the Choi state $\rho_{\mathcal{E}}$. Let $\{\mathcal{W}_1, \dots, \mathcal{W}_m\}$ be independent Pauli observables, each of the form $\mathcal{W}_i = P_i^S \otimes P_i^A$, sampled uniformly at random from the bases set $\{\mathcal{W}_1, \dots, \mathcal{W}_{d^4}\}$.

Define the linear map $\Lambda: \mathbb{C}^{d^2 \times d^2} \rightarrow \mathbb{R}^m$ as

$$(\Lambda(\rho_{\mathcal{E}}))_i = \sqrt{\frac{d^2}{m}} \text{Tr}(\mathcal{W}_i \rho_{\mathcal{E}}), \quad (6)$$

and consider the measurement model

$$\mathbf{y} = \Lambda(\rho_{\mathcal{E}}) + \mathbf{v} + \mathbf{z}, \quad (7)$$

where \mathbf{v} represents the sparse corrupted noise with $\|\mathbf{v}\|_0 \leq s$, and \mathbf{z} is the measurement noise. We denote the extended matrix by $\mathcal{M} = [\Lambda, I] \in \mathbb{C}^{m \times (d^4+m)}$, and then derive the conditions under which \mathcal{M} satisfies the generalized restricted isometry property.

Proposition 1. Let $\delta \in [0, 1]$. If

$$m \geq C_1 r d^2 \log^6 d, \quad \text{and} \quad \sup \|\mathbf{v}\|_{\infty} \leq \frac{\delta}{4d\sqrt{s}}, \quad (8)$$

for some constant $C_1 = O(1/\delta^2)$, then with high probability, the extended measurement matrix $\mathcal{M} = [\Lambda, I]$ satisfies the GRIP with constant $\delta_{r,s} \leq \delta$.

Proof. Similar to the proof in Appendix A, the GRIP constant $\delta_{r,s}$ can be equivalently expressed as

$$\delta_{r,s} = \sup_{(\rho_{\mathcal{E}}, \mathbf{v})} \left| \left\| \mathcal{M} \begin{bmatrix} \rho_{\mathcal{E}} \\ \mathbf{v} \end{bmatrix} \right\|_2^2 - \|\rho_{\mathcal{E}}\|_F^2 - \|\mathbf{v}\|_2^2 \right|, \quad (9)$$

where the supremum is taken over rank- r matrices $\rho_{\mathcal{E}} \in \mathbb{C}^{d^2 \times d^2}$ and s -sparse vectors $\mathbf{v} \in \mathbb{R}^m$. We split the expression as

$$\delta_{r,s} \leq \underbrace{\sup_{(\rho_{\mathcal{E}}, \mathbf{v})} \left| \|\Lambda(\rho_{\mathcal{E}})\|_2^2 - \|\rho_{\mathcal{E}}\|_F^2 \right|}_{\delta_1} + \underbrace{\sup_{(\rho_{\mathcal{E}}, \mathbf{v})} |\langle \Lambda(\rho_{\mathcal{E}}), \mathbf{v} \rangle|}_{\delta_2}. \quad (10)$$

From the known RIP results, $\delta_1 \leq \delta/2$ holds with high probability if $m \geq C_1 r d^2 \log^6 d$. For δ_2 , we note that $|\text{Tr}(\mathcal{W}_i \rho_{\mathcal{E}})| \leq 1$, and

$$\sup \|\mathbf{v}\|_2 \leq \sup \sqrt{s} \|\mathbf{v}\|_{\infty}, \quad (11)$$

where $\|\mathbf{v}\|_{\infty} = \max_i |v_i|$. Therefore,

$$\delta_2 \leq 2\sqrt{\frac{d^2}{m}} \cdot \sqrt{ms} \cdot \sup \|\mathbf{v}\|_{\infty} = 2d\sqrt{s} \sup \|\mathbf{v}\|_{\infty}. \quad (12)$$

To ensure $\delta_2 \leq \delta/2$, it suffices that

$$\sup \|\mathbf{v}\|_{\infty} \leq \frac{\delta}{4d\sqrt{s}}. \quad (13)$$

Combining both bounds yields $\delta_{r,s} \leq \delta$. \square

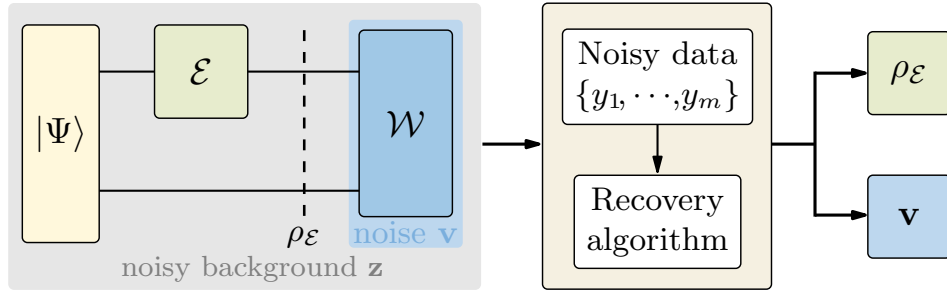


FIG. 1. Schematic procedure of the corrupted sensing QPT based on the Choi-state representation. The maximally entangled state $|\Psi\rangle$ is prepared and sent into the quantum process \mathcal{E} . The output Choi state $\rho_{\mathcal{E}}$ is then measured to obtain the noisy data $\mathbf{y} = \{y_1, \dots, y_m\}$. We randomly select m Pauli observables $\{\mathcal{W}_1, \dots, \mathcal{W}_m\}$, with $m \leq d^4$. By using the recovery algorithm, the Choi state $\rho_{\mathcal{E}}$ and the measurement noise \mathbf{v} can be reconstructed simultaneously, and \mathbf{z} denotes any other potential noise.

B. The estimator

We can solve the following problem to recover the Choi state $\rho_{\mathcal{E}}$ and sparse noise \mathbf{v} simultaneously:

$$\begin{aligned} \min_{\rho'_{\mathcal{E}}, \mathbf{v}'} & \frac{1}{2} \|\mathbf{y} - \tilde{\Lambda}(\rho'_{\mathcal{E}}) - \mathbf{v}'\|_2^2 + \tau_1 \cdot \|\rho'_{\mathcal{E}}\|_{\text{tr}} + \tau_2 \cdot \|\mathbf{v}'\|_1, \\ \text{s.t. } & \rho'_{\mathcal{E}} \succeq 0, \text{Tr}_S(\rho'_{\mathcal{E}}) = \frac{I}{d}, \\ & \tau_1, \tau_2 > 0. \end{aligned} \quad (14)$$

Here, $\tilde{\Lambda}(\rho'_{\mathcal{E}})$ omits the factor $\sqrt{d^2/m}$ from Eq. (6), as this factor is not necessary for the estimator to work [34]. The trace norm (or nuclear norm) of X is defined as $\|X\|_{\text{tr}} = \text{Tr}(\sqrt{X^\dagger X})$, and $\rho'_{\mathcal{E}}$ and \mathbf{v}' are the optimization variables. It is worth noting that the positive semidefinite constraint on the Choi state and the trace-preserving constraint of the quantum channel together lead to the Choi state having a constant trace norm. Therefore, the trace norm term in Eq. (14) can be omitted without significantly affecting the results [23]. The schematic framework is illustrated in Fig. 1.

To evaluate the reconstruction quality of the Choi state $\hat{\rho}_{\mathcal{E}}$ and the sparse noise $\hat{\mathbf{v}}$, we adopt two standard measures. The first is the (squared) fidelity [14, 35], defined as

$$F(\hat{\rho}_{\mathcal{E}}, \rho_{\mathcal{E}}) = \left(\text{Tr} \sqrt{\hat{\rho}_{\mathcal{E}}^{1/2} \rho_{\mathcal{E}} \hat{\rho}_{\mathcal{E}}^{1/2}} \right)^2, \quad (15)$$

which evaluates how close the estimated Choi state $\hat{\rho}_{\mathcal{E}}$ is to the true state $\rho_{\mathcal{E}}$. The second measure is the mean squared error (MSE),

$$T_{\text{MSE}} = \frac{1}{m} \sum_{i=1}^m (\mathbf{v}_i - \hat{\mathbf{v}}_i)^2, \quad (16)$$

which quantifies the discrepancy between the estimated sparse noise $\hat{\mathbf{v}}$ and the true noise \mathbf{v} .

C. Applications

Recall that the maximally entangled state is written as $|\Psi\rangle = \frac{1}{\sqrt{d}} \sum_{j=0}^{d-1} |j\rangle \otimes |j\rangle$, and the corresponding density operator is $\rho = |\Psi\rangle\langle\Psi|$. Let $U \in \mathbb{C}^{d \times d}$ be a unitary operator acting on the n -qubit system. Then, the Choi state associated with the unitary channel $\mathcal{E}(\cdot) = U(\cdot)U^\dagger$ can be written as

$$\rho_{\mathcal{E}} = (U \otimes I_d) \rho (U^\dagger \otimes I_d), \quad (17)$$

where I_d denotes the identity operator on the d -dimensional Hilbert space. Since the conclusion of Proposition 1 is essentially a worst-case scenario, $\|\mathbf{v}\|_\infty$ is bounded. In the numerical simulations, however, we adopt a more realistic model by using s -sparse Gaussian noise with zero mean and unit variance, where $s = \lfloor \eta m \rfloor$.

For two-qubit gates, as illustrated in Fig. 2 for the CNOT gate with sparsity ratios $\eta = 0.05$ and $\eta = 0.1$, the fidelity F (and the mean squared error T_{MSE}) increase (decrease) with the number of sampled Pauli observables m , thereby confirming the effectiveness of the method. When $\eta = 0.05$, the overall performance in terms of fidelity and T_{MSE} is better than that in the case of $\eta = 0.1$. The measurement data are obtained using 10^3 independent trials for each measurement setting, with finite-sampling noise absorbed into \mathbf{z} . However, the Choi-state scheme based on Pauli observables does not make effective use of the sampled observables. Therefore, in Sec. III we conduct a more detailed numerical study using the process-matrix scheme. For instance, for the CNOT gate, $m = 192$ is required to reach a fidelity of $F(\hat{\rho}_{\mathcal{E}_{\text{cn}}}, \rho_{\mathcal{E}_{\text{cn}}}) \approx 0.9506$ under $\eta = 0.1$, with an MSE of $T_{\text{MSE}} \approx 7.66 \times 10^{-4}$. In contrast, as shown in Sec. III C, a fidelity of $F(\hat{\chi}_{\text{cn}}, \chi_{\text{cn}}) \approx 0.958$ can be achieved using only 64 configurations.

Beyond two-qubit gates, we turn to the three-qubit Toffoli gate. The Toffoli gate, also known as the CCNOT gate, inverts the target qubit (third qubit) if the first and

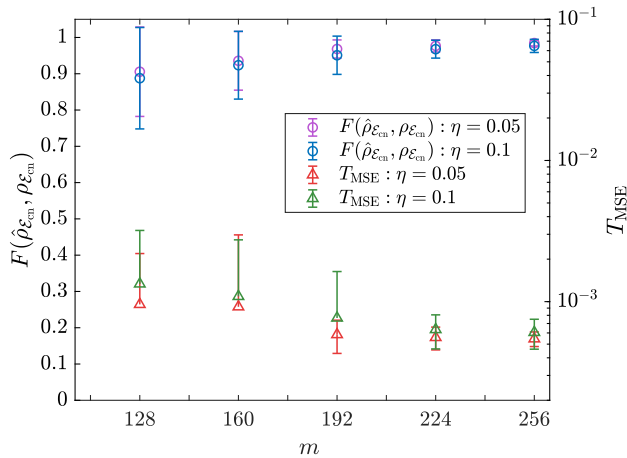


FIG. 2. Fidelity $F(\hat{\rho}_{\mathcal{E}_{\text{cn}}}, \rho_{\mathcal{E}_{\text{cn}}})$ and MSE T_{MSE} as functions of the number of sampled Pauli observables \mathcal{W} (denoted by m). The error bars are obtained from 100 runs of tomography, with each run selecting m Pauli observables randomly. The purple and blue points represent the fidelity between the reconstructed Choi state and true Choi state of the CNOT gate, for sparsity ratios $\eta = 0.05$ and 0.1 , respectively. The red and green points show the MSE between the reconstructed sparse Gaussian noise and true sparse Gaussian noise, for sparsity ratios $\eta = 0.05$ and 0.1 , respectively. The Gaussian noise has a mean of zero, a standard deviation of 1. The regularization parameters are chosen as $\tau_1 = 0.01m$, $\tau_2 = 10^{-2}$.

second qubits are both $|1\rangle$, namely,

$$U_{\text{Tof}} = |0\rangle\langle 0| \otimes I \otimes I + |1\rangle\langle 1| \otimes U_{\text{CNOT}}. \quad (18)$$

For reference, Fig. 3 presents the results for the three-qubit Toffoli gate. When $m \gtrsim 3072$, the fidelity $F(\hat{\rho}_{\mathcal{E}_{\text{Tof}}}, \rho_{\mathcal{E}_{\text{Tof}}}) \gtrsim 0.95$; however, even at $m = 4096$, the fidelity attains 0.9631 under $\eta = 0.05$. Correspondingly, the process-matrix scheme is presented in Sec. III D.

III. CORRUPTED SENSING QUANTUM PROCESS TOMOGRAPHY VIA PROCESS MATRIX

A. The process-matrix representation

In the Kraus representation, a completely positive (CP) map \mathcal{E} is written as

$$\mathcal{E}(\rho) = \sum_i E_i \rho E_i^\dagger, \quad (19)$$

where $\{E_i\}$ are the Kraus operators. The map is trace preserving (TP) when $\sum_i E_i^\dagger E_i = I$. Usually it is more convenient to consider an equivalent description of \mathcal{E} , where the process-matrix representation of \mathcal{E} can be obtained by writing the Kraus operators in a certain set of bases $\Gamma_\alpha \in \mathbb{C}^{d \times d}$ such that $E_i = \sum_{\alpha=1}^{d^2} e_{i\alpha} \Gamma_\alpha$, for some complex numbers $e_{i\alpha}$. Then the process-matrix repre-

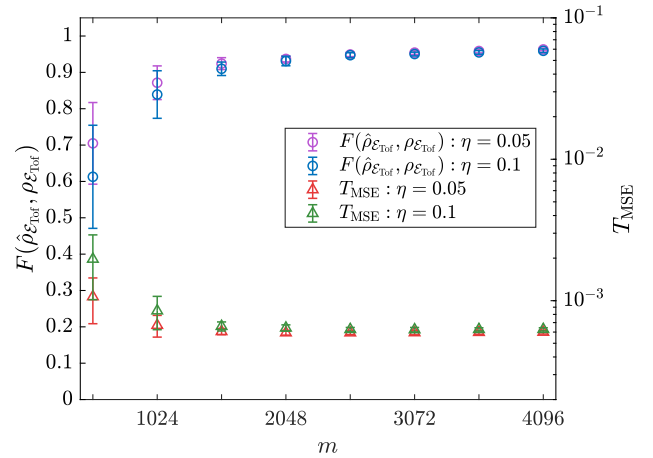


FIG. 3. Fidelity $F(\hat{\rho}_{\mathcal{E}_{\text{Tof}}}, \rho_{\mathcal{E}_{\text{Tof}}})$ and MSE T_{MSE} as functions of the number of sampled Pauli observables \mathcal{W} (denoted by m). The error bars are obtained from 50 runs of tomography, with each run selecting m Pauli observables randomly. The purple and blue points represent the fidelity between the reconstructed Choi state and true Choi state of Toffoli gate, for sparsity ratios $\eta = 0.05$ and 0.1 , respectively. The red and green points show the MSE between the reconstructed sparse Gaussian noise and true sparse Gaussian noise, for sparsity ratios $\eta = 0.05$ and 0.1 , respectively. The Gaussian noise has a mean of zero, a standard deviation of 1. The regularization parameters are chosen as $\tau_1 = 0.01m$, $\tau_2 = 10^{-2}$.

sentation can be expressed as

$$\mathcal{E}(\rho) = \sum_{\alpha, \beta=1}^{d^2} \chi_{\alpha\beta} \Gamma_\alpha \rho \Gamma_\beta^\dagger, \quad (20)$$

where $\chi_{\alpha\beta} = \sum_i e_{i\alpha} e_{i\beta}^*$ are the elements of the $d^2 \times d^2$ process matrix in the Γ_α bases for a system of n qubits and $d = 2^n$. The process matrix is a positive-semidefinite matrix (implying that it is Hermitian), and satisfies the TP condition:

$$\chi \succ 0, \quad (21)$$

$$\sum_{\alpha, \beta=1}^{d^2} \chi_{\alpha \beta} \Gamma_\beta^\dagger \Gamma_\alpha = I. \quad (22)$$

Hence, if the Γ_α bases fulfill $\text{Tr}(\Gamma_\beta^\dagger \Gamma_\alpha) = \delta_{\alpha\beta}$, $\text{Tr}(\chi) = d$, and $\text{Tr}(\Gamma_\beta^\dagger \Gamma_\alpha) = d\delta_{\alpha\beta}$, then $\text{Tr}(\chi) = 1$.

Given that any representation of a general map has $d^2(d^2 - 1)$ independent parameters, the specification of such a map can be accomplished by probing it with d^2 input states ρ^{in} , forming a set of Hermitian operator bases. An informationally complete measurement on the resulting output state $\mathcal{E}(\rho^{\text{in}})$ reveals $d^2 - 1$ independent parameters that characterize the map.

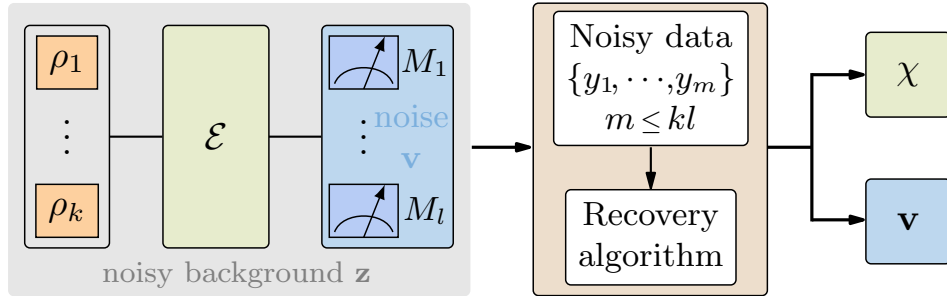


FIG. 4. Schematic procedure of the corrupted sensing QPT based on the process-matrix representation. Consider preparing different initial states ρ_o , applying the process \mathcal{E} , and then measuring the outputs using a set of observables M_o to get the noisy data $\mathbf{y}: \{y_1, \dots, y_m\}$. Here, we select m configurations $(\rho_o, M_o), o = 1, \dots, m \leq kl$ randomly. By using the recovery algorithm, the process matrix χ and the measurement noise \mathbf{v} can be reconstructed simultaneously, and \mathbf{z} denotes any other potential noise.

B. Problem formulation

Consider preparing different initial input states $\{\rho_1, \dots, \rho_k\}$, applying the process \mathcal{E} , and then measuring the outputs using the observable M from the set $\{M_1, \dots, M_l\}$. For a pair $(\rho_o, M_o), o = 1, \dots, m \leq kl$, the presence of noise in the measurement process might corrupt the measurement data. Consequently, the outcome can be expressed as

$$\mathbf{y} = \Phi\chi + \mathbf{v} + \mathbf{z}, \quad (23)$$

where $\chi \in \mathbb{C}^{d^4 \times 1}$ is the vectorized form of the process matrix χ in the $\{\Gamma_\alpha\}$ bases, Φ is an $m \times d^4$ matrix with elements of the form $\text{Tr}(\Gamma_\alpha \rho_o \Gamma_\beta^\dagger M_o) / \sqrt{m}$. And the corrupted noise is considered as a structured vector $\mathbf{v} \in \mathbb{R}^m$, and $\mathbf{z} \in \mathbb{R}^m$ is any other kind of unstructured noise.

If we assume the process matrix χ being sparse in any known basis, and the noise as a sparse vector \mathbf{v} , the following problem can be solved to recover χ and \mathbf{v} simultaneously:

$$\begin{aligned} \min_{\chi', \mathbf{v}'} & \frac{1}{2} \|\mathbf{y} - \Phi\chi' - \mathbf{v}'\|_2^2 + \mu_1 \cdot \|\chi'\|_1 + \mu_2 \cdot \|\mathbf{v}'\|_1, \\ \text{s.t. } & \chi' \succeq 0, \sum_{\alpha, \beta} \chi'_{\alpha \beta} \Gamma_\beta^\dagger \Gamma_\alpha = I, \\ & \mu_1, \mu_2 > 0. \end{aligned} \quad (24)$$

The schematic framework is shown in Fig. 4.

C. Two-qubit entangling gates

Consider encoding the qubits in polarization states with $|H\rangle = |0\rangle$, $|V\rangle = |1\rangle$, and $|D(A)\rangle = (|H\rangle \pm |V\rangle)/\sqrt{2}$, $|R(L)\rangle = (|H\rangle \pm i|V\rangle)/\sqrt{2}$. For a two-qubit gate, standard process tomography requires 256 different settings of input states and measurement projectors. There is significant flexibility in selecting the tomographic input and measurement settings. As one

accessible choice, our input states ρ are chosen from $\{HH, VH, DV, RH, RV, VV, HV, HA, HR, RR, RA, DA, DL, VA, VR, DH\}$ and the measurements M are from $\{HH, HV, VH, VV, HD, HR, VR, VD, DD, LR, LD, DL, DV, LV, DH, LH\}$. In total, there are $16 \times 16 = 256$ configurations of the (ρ, M) pairs.

We employ two approaches for the numerical calculations using MATLAB: the results for the two-qubit gates in this section are obtained using the cvx [36] package with the solver SDPT3, while for larger scales, the results presented in Secs. III D and III E use the cvx package with the solver MOSEK to achieve more stable solutions. Here, by randomly selecting $m \leq 256$ configurations from all combinations, the process matrix χ and corrupted noise \mathbf{v} can be obtained simultaneously by solving Eq. (24). The process matrices in the Pauli bases for the CNOT, CZ, and SWAP gates are given in Appendix B 1. Using the Pauli bases set $\{\Gamma_\alpha^{\text{Pau}}\}$, we assess the reconstruction of each gate by means of the fidelity $F(\hat{\chi}, \chi)$ and the mean squared error T_{MSE} , as shown in Fig. 5 and Fig. 8 in Appendix B 1.

For the CNOT gate, a fidelity of $F(\hat{\chi}_{\text{cn}}, \chi_{\text{cn}}) \approx 0.962$ is achieved with $m = 64$ configurations, corresponding to an MSE of $T_{\text{MSE}} \approx 2 \times 10^{-4}$. Similarly, the two-qubit CZ gate requires only $m = 64$ configurations to achieve $F(\hat{\chi}_{\text{cz}}, \chi_{\text{cz}}) \approx 0.971$, corresponding to $T_{\text{MSE}} \approx 1.368 \times 10^{-4}$. Finally, the SWAP gate reaches $F(\hat{\chi}_{\text{sw}}, \chi_{\text{sw}}) \approx 0.978$ at $m = 48$ (i.e., a sampling rate of 18.75%), with $T_{\text{MSE}} \approx 1.55 \times 10^{-4}$.

D. Three-qubit gates

In this section, we prepare pairwise combinations of the 64 inputs $\{|H\rangle, |V\rangle, |D\rangle, |R\rangle\}^{\otimes 3}$ and 64 observables $\{|H\rangle, |V\rangle, |D\rangle, |R\rangle\}^{\otimes 3}$, and then randomly select $m \leq 4096$ configurations from all $d^4 = 4096$ possible combinations. The process matrix in the Pauli bases of the Toffoli gate is given in Appendix B 2. With the Pauli bases set $\{\Gamma_\alpha^{\text{Pau}}\}$, we assess the reconstruction by

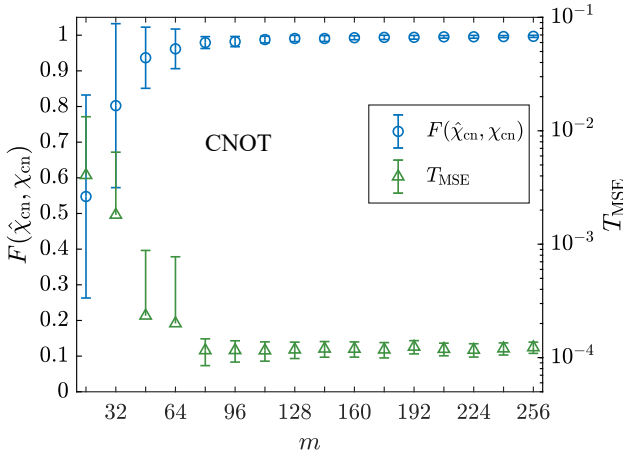


FIG. 5. Fidelity $F(\hat{\chi}_{\text{cn}}, \chi_{\text{cn}})$ and MSE T_{MSE} as functions of the number of configurations m . The error bars are obtained from 100 runs of tomography, with each run selecting m combinations randomly. The blue points represent the fidelity between the reconstructed process matrix and true process matrix of the CNOT gate. The green points show the MSE between the reconstructed sparse Gaussian noise and true sparse Gaussian noise. The Gaussian noise has a mean of zero, a standard deviation of 1, and a sparsity level of $s = \lfloor 0.1m \rfloor$. The regularization parameters are chosen as $\mu_1 = 10^{-5}$, $\mu_2 = 10^{-3}$.

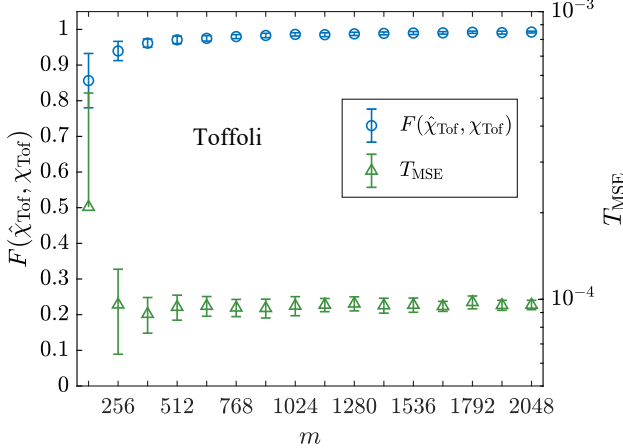


FIG. 6. Fidelity $F(\hat{\chi}_{\text{Tof}}, \chi_{\text{Tof}})$ and MSE T_{MSE} as functions of the number of configurations m . The error bars are obtained from 50 runs of tomography, with each run selecting m combinations randomly. The blue points represent the fidelity between the reconstructed process matrix and true process matrix of the Toffoli gate. The green points show the MSE between the reconstructed sparse Gaussian noise and true sparse Gaussian noise. The Gaussian noise has a mean of zero, a standard deviation of 1, and a sparsity level of $s = \lfloor 0.1m \rfloor$. The regularization parameters are chosen as $\mu_1 = 10^{-5}$, $\mu_2 = 10^{-3}$.

means of $F(\hat{\chi}_{\text{Tof}}, \chi_{\text{Tof}})$ and T_{MSE} ; see Fig. 6.

The three-qubit Toffoli gate requires lower sampling compared to two-qubit gates to achieve comparable fidelities: a fidelity of $F(\hat{\chi}_{\text{Tof}}, \chi_{\text{Tof}}) \approx 0.9615$ is already achieved at $m = 384$ (i.e., a sampling rate of 9.375%),

with an MSE of $T_{\text{MSE}} \approx 8.89 \times 10^{-5}$, highlighting the scalability of the method under increased system size. Furthermore, when $m = 1664$ (corresponding to a sampling rate of 40.625%), the fidelity reaches 0.99.

The Fredkin gate or the three-qubit conditional SWAP gate swaps the last two qubits if the first qubit is $|1\rangle$, namely,

$$U_{\text{Fred}} = |0\rangle\langle 0| \otimes I \otimes I + |1\rangle\langle 1| \otimes U_{\text{SWAP}}. \quad (25)$$

The process matrix in the Pauli bases of the Fredkin gate is given in Appendix B2. With the Pauli bases set $\{\Gamma_\alpha^{\text{Pau}}\}$, we assess the reconstruction by means of $F(\hat{\chi}_{\text{Fred}}, \chi_{\text{Fred}})$ and T_{MSE} ; see Fig. 9 in Appendix B2.

The process matrix of the Fredkin gate is reconstructed with a fidelity of $F(\hat{\chi}_{\text{Fred}}, \chi_{\text{Fred}}) \approx 0.9553$ at $m = 256$ (i.e., a sampling rate of 6.25%), accompanied by an MSE of $T_{\text{MSE}} \approx 9.2 \times 10^{-5}$. The fidelity is further improved to $F(\hat{\chi}_{\text{Fred}}, \chi_{\text{Fred}}) \approx 0.99$ when the sampling rate reaches 37.5%.

E. Four-qubit CCCZ gate

The x -controlled Z gate, also denoted as C^xZ , applies a Z -gate to the target qubit controlled by x qubits. For $x = 3$, it is commonly referred to as the $CCCZ$ gate [37–39], a typical four-qubit gate, given by the expression:

$$U_{\text{CC CZ}} = I - 2|1111\rangle\langle 1111|. \quad (26)$$

In this section, we prepare pairwise combinations of the $d^2 = 256$ inputs $\{|H\rangle, |V\rangle, |D\rangle, |R\rangle\}^{\otimes 4}$ and d^2 observables $\{|H\rangle, |V\rangle, |D\rangle, |R\rangle\}^{\otimes 4}$, and then randomly select $m \ll d^4$ configurations from all possible combinations. The process matrix of the CCCZ gate in the Pauli bases is given in Appendix B3. With the Pauli bases set $\{\Gamma_\alpha^{\text{Pau}}\}$, we assess the reconstruction by means of $F(\hat{\chi}_{\text{ccc}z}, \chi_{\text{ccc}z})$ and T_{MSE} ; see Fig. 7.

The four-qubit $CCCZ$ gate requires the lowest sampling: a sampling rate of 3.125% ($m = 2048$) yields a fidelity of $F(\hat{\chi}_{cccZ}, \chi_{cccZ}) \approx 0.971$, with an MSE of $T_{\text{MSE}} \approx 5.77 \times 10^{-5}$. The fidelity can be improved to $F(\hat{\chi}_{cccZ}, \chi_{cccZ}) \approx 0.9945$ at $m = 16384$ (i.e., a sampling rate of 25%), which further demonstrates the method's scalability to larger systems.

IV. SUMMARY

In this work, we have proposed a corrupted sensing framework for quantum process tomography that enables the simultaneous reconstruction of quantum processes and sparse measurement noise. By introducing the generalized restricted isometry property for the Choi-state representation, we established a probabilistic condition under which the extended measurement matrix satisfies the GRIP with high probability.

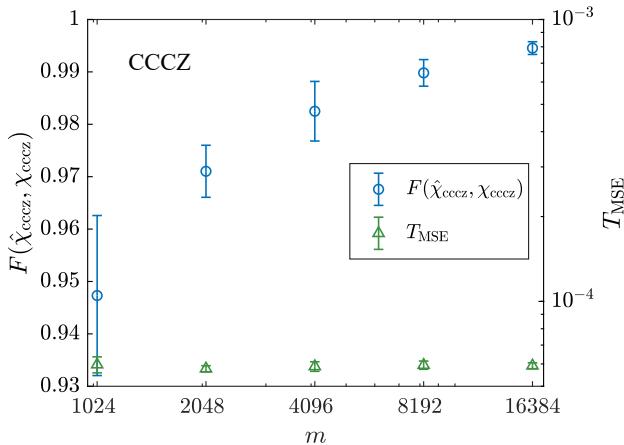


FIG. 7. Fidelity $F(\hat{X}_{\text{cccz}}, \chi_{\text{cccz}})$ and MSE T_{MSE} as functions of the number of configurations m . The error bars are obtained from 10 runs of tomography, with each run selecting m combinations randomly. The blue points represent the fidelity between the reconstructed process matrix and true process matrix of the CCCZ gate. The green points show the MSE between the reconstructed sparse Gaussian noise and true sparse Gaussian noise. The Gaussian noise has a mean of zero, a standard deviation of 1, and a sparsity level of $s = \lfloor 0.1m \rfloor$. The regularization parameters are chosen as $\mu_1 = 10^{-5}$, $\mu_2 = 10^{-3}$.

Furthermore, systematic numerical simulations of several typical quantum gates were conducted in the

process-matrix representation to validate the effectiveness of the method. In comparison with the Choi-state scheme, which selects random Pauli operators, the process-matrix approach utilizes the selected input-output measurement configurations more efficiently. The results show that the four-qubit CCCZ gate requires the lowest sampling rate to reach the fidelity threshold, highlighting the scalability of the method in handling larger multi-qubit systems.

Several aspects merit further investigation. First, based on the established GRIP condition, deriving explicit error bounds would offer a more complete theoretical guarantee for the proposed corrupted sensing framework. In addition, since the GRIP is a strong property for low-rank matrices and sparse noise, alternative analytical tools may be explored to provide theoretical insights. Finally, measurement tomography in the corrupted sensing setting can be considered.

ACKNOWLEDGMENTS

We thank Yinfei Li and Ye-Chao Liu for helpful discussions. We are also grateful to Yulong Liu, Yanwu Gu and Zhenpeng Xu for inspiring discussions at an earlier stage of this project. This work was supported by the National Natural Science Foundation of China (Grants No. 92265115 and No. 12175014) and the National Key R&D Program of China (Grant No. 2022YFA1404900).

[1] M. A. Nielsen and I. L. Chuang, *Quantum Computation and Quantum Information* (Cambridge University Press, 2010).

[2] J. B. Altepeter, D. Branning, E. Jeffrey, T. C. Wei, P. G. Kwiat, R. T. Thew, J. L. O'Brien, M. A. Nielsen, and A. G. White, Ancilla-assisted quantum process tomography, *Phys. Rev. Lett.* **90**, 193601 (2003).

[3] J. L. O'Brien, G. J. Pryde, A. Gilchrist, D. F. V. James, N. K. Langford, T. C. Ralph, and A. G. White, Quantum process tomography of a controlled-NOT gate, *Phys. Rev. Lett.* **93**, 080502 (2004).

[4] M. Mohseni and D. A. Lidar, Direct characterization of quantum dynamics, *Phys. Rev. Lett.* **97**, 170501 (2006).

[5] M. Lobino, D. Korystov, C. Kupchak, E. Figueira, B. C. Sanders, and A. I. Lvovsky, Complete characterization of quantum-optical processes, *Science* **322**, 563 (2008).

[6] M. Mohseni, A. T. Rezakhani, and D. A. Lidar, Quantum-process tomography: Resource analysis of different strategies, *Phys. Rev. A* **77**, 032322 (2008).

[7] V. Gebhart, R. Santagati, A. A. Gentile, E. M. Gauger, D. Craig, N. Ares, L. Banchi, F. Marquardt, L. Pezze, and C. Bonato, Learning quantum systems, *Nat. Rev. Phys.* **5**, 141 (2023).

[8] J. Emerson, M. Silva, O. Moussa, C. Ryan, M. Laforest, J. Baugh, D. G. Cory, and R. Laflamme, Symmetrized characterization of noisy quantum processes, *Science* **317**, 1893 (2007).

[9] A. Bendersky, F. Pastawski, and J. P. Paz, Selective and efficient estimation of parameters for quantum process tomography, *Phys. Rev. Lett.* **100**, 190403 (2008).

[10] M. P. A. Branderhorst, J. Nunn, I. A. Walmsley, and R. L. Kosut, Simplified quantum process tomography, *New J. Phys.* **11**, 115010 (2009).

[11] E. Knill, D. Leibfried, R. Reichle, J. Britton, R. B. Blakestad, J. D. Jost, C. Langer, R. Ozeri, S. Seidelin, and D. J. Wineland, Randomized benchmarking of quantum gates, *Phys. Rev. A* **77**, 012307 (2008).

[12] E. Magesan, J. M. Gambetta, B. R. Johnson, C. A. Ryan, J. M. Chow, S. T. Merkel, M. P. da Silva, G. A. Keefe, M. B. Rothwell, T. A. Ohki, M. B. Ketchen, and M. Steffen, Efficient measurement of quantum gate error by interleaved randomized benchmarking, *Phys. Rev. Lett.* **109**, 080505 (2012).

[13] I. Roth, R. Kueng, S. Kimmel, Y.-K. Liu, D. Gross, J. Eisert, and M. Kliesch, Recovering quantum gates from few average gate fidelities, *Phys. Rev. Lett.* **121**, 170502 (2018).

[14] S. T. Flammia and Y.-K. Liu, Direct fidelity estimation from few Pauli measurements, *Phys. Rev. Lett.* **106**, 230501 (2011).

[15] M. P. da Silva, O. Landon-Cardinal, and D. Poulin, Practical characterization of quantum devices without tomography, *Phys. Rev. Lett.* **107**, 210404 (2011).

[16] L. Steffen, M. P. da Silva, A. Fedorov, M. Baur, and A. Wallraff, Experimental Monte Carlo quantum process

certification, *Phys. Rev. Lett.* **108**, 260506 (2012).

[17] D. Gross, Y.-K. Liu, S. T. Flammia, S. Becker, and J. Eisert, Quantum state tomography via compressed sensing, *Phys. Rev. Lett.* **105**, 150401 (2010).

[18] C. A. Riofrio, D. Gross, S. T. Flammia, T. Monz, D. Nigg, R. Blatt, and J. Eisert, Experimental quantum compressed sensing for a seven-qubit system, *Nat. Commun.* **8**, 15305 (2017).

[19] A. Shabani, R. L. Kosut, M. Mohseni, H. Rabitz, M. A. Broome, M. P. Almeida, A. Fedrizzi, and A. G. White, Efficient measurement of quantum dynamics via compressive sensing, *Phys. Rev. Lett.* **106**, 100401 (2011).

[20] S. T. Flammia, D. Gross, Y.-K. Liu, and J. Eisert, Quantum tomography via compressed sensing: error bounds, sample complexity and efficient estimators, *New J. Phys.* **14**, 095022 (2012).

[21] C. H. Baldwin, A. Kalev, and I. H. Deutsch, Quantum process tomography of unitary and near-unitary maps, *Phys. Rev. A* **90**, 012110 (2014).

[22] A. V. Rodionov, A. Veitia, R. Barends, J. Kelly, D. Sank, J. Wenner, J. M. Martinis, R. L. Kosut, and A. N. Korotkov, Compressed sensing quantum process tomography for superconducting quantum gates, *Phys. Rev. B* **90**, 144504 (2014).

[23] M. Kliesch, R. Kueng, J. Eisert, and D. Gross, Guaranteed recovery of quantum processes from few measurements, *Quantum* **3**, 171 (2019).

[24] M. Cramer, M. B. Plenio, S. T. Flammia, R. Somma, D. Gross, S. D. Bartlett, O. Landon-Cardinal, D. Poulin, and Y.-K. Liu, Efficient quantum state tomography, *Nat. Commun.* **1**, 149 (2010).

[25] T. Baumgratz, D. Gross, M. Cramer, and M. B. Plenio, Scalable reconstruction of density matrices, *Phys. Rev. Lett.* **111**, 020401 (2013).

[26] B. P. Lanyon, C. Maier, M. Holzäpfel, T. Baumgratz, C. Hempel, P. Jurcevic, I. Dhand, A. Buyskikh, A. J. Daley, M. Cramer, *et al.*, Efficient tomography of a quantum many-body system, *Nat. Phys.* **13**, 1158 (2017).

[27] J. I. Cirac, D. Pérez-García, N. Schuch, and F. Verstraete, Matrix product states and projected entangled pair states: Concepts, symmetries, theorems, *Rev. Mod. Phys.* **93**, 045003 (2021).

[28] G. Torlai, C. J. Wood, A. Acharya, G. Carleo, J. Carrasquilla, and L. Aolita, Quantum process tomography with unsupervised learning and tensor networks, *Nat. Commun.* **14**, 2858 (2023).

[29] M. Ma and J. Shang, Corrupted sensing quantum state tomography, *New J. Phys.* **27**, 054501 (2025).

[30] B. Recht, M. Fazel, and P. A. Parrilo, Guaranteed minimum-rank solutions of linear matrix equations via nuclear norm minimization, *SIAM Review* **52**, 471 (2010).

[31] P. Zhang, L. Gan, C. Ling, and S. Sun, Uniform recovery bounds for structured random matrices in corrupted compressed sensing, *IEEE Trans. Signal Process.* **66**, 2086 (2018).

[32] A. Jamiołkowski, Linear transformations which preserve trace and positive semidefiniteness of operators, *Rep. Math. Phys.* **3**, 275 (1972).

[33] M.-D. Choi, Completely positive linear maps on complex matrices, *Linear Algebr. Appl.* **10**, 285 (1975).

[34] M.-C. Hsu, E.-J. Kuo, W.-H. Yu, J.-F. Cai, and M.-H. Hsieh, Quantum state tomography via nonconvex riemannian gradient descent, *Phys. Rev. Lett.* **132**, 240804 (2024).

[35] R. Jozsa, Fidelity for mixed quantum states, *J. Mod. Opt.* **41**, 2315 (1994).

[36] M. Grant and S. Boyd, CVX: MATLAB software for disciplined convex programming, version 2.1, <https://cvxr.com/cvx> (2014).

[37] S. S. Ivanov, P. A. Ivanov, and N. V. Vitanov, Efficient construction of three- and four-qubit quantum gates by global entangling gates, *Phys. Rev. A* **91**, 032311 (2015).

[38] C. Song, S.-B. Zheng, P. Zhang, K. Xu, L. Zhang, Q. Guo, W. Liu, D. Xu, H. Deng, K. Huang, *et al.*, Continuous-variable geometric phase and its manipulation for quantum computation in a superconducting circuit, *Nat. Commun.* **8**, 1061 (2017).

[39] J. Huang, X. Li, X. Chen, C. Zhai, Y. Zheng, Y. Chi, Y. Li, Q. He, Q. Gong, and J. Wang, Demonstration of hypergraph-state quantum information processing, *Nat. Commun.* **15**, 2601 (2024).

[40] Y.-K. Liu, Universal low-rank matrix recovery from Pauli measurements, *Adv. Neural Inf. Proc. Sys.* **24**, 1638 (2011).

Appendix A: The GRIP condition for corrupted sensing quantum state tomography

Consider an n -qubit quantum system with dimension $d = 2^n$, the unknown state of the system is denoted by ρ , which satisfies $\text{Tr}(\rho) = 1$ and $\rho \succeq 0$. An n -qubit Pauli operator takes on the general form

$$W = \bigotimes_{i=1}^n \sigma_i, \quad (\text{A1})$$

where $\sigma_i \in \{I, \sigma_x, \sigma_y, \sigma_z\}$. Here, $\sigma_x, \sigma_y, \sigma_z$ are the three Pauli matrices, and I represents the identity matrix. The density matrix ρ can be expanded by using the Pauli observables $\{W_i: i \in [d^2]\}$. By choosing m elements $\{P_1, P_2, \dots, P_m\}$ uniformly at random from the Pauli bases set $\{W_1, W_2, \dots, W_{d^2}\}$, the i -th component $(\mathcal{A}(\rho))_i$ of the linear map $\mathcal{A}: \mathbb{C}^{d \times d} \rightarrow \mathbb{R}^m$ for Pauli measurements can be defined as

$$(\mathcal{A}(\rho))_i = \sqrt{\frac{d}{m}} \text{Tr}(P_i \rho) \quad (\text{A2})$$

for $\rho \in \mathbb{C}^{d \times d}$. The corresponding adjoint operator $\mathcal{A}^\dagger: \mathbb{R}^m \rightarrow \mathbb{C}^{d \times d}$ is

$$\mathcal{A}^\dagger(\mathbf{y}) = \sqrt{\frac{d}{m}} \sum_{i=1}^m y_i P_i, \quad (\text{A3})$$

where $\mathbf{y} \in \mathbb{R}^m$. The coefficient $\sqrt{d/m}$ is chosen so that $\mathbb{E}[\mathcal{A}^\dagger(\mathcal{A}(\rho))] = \rho$.

Proposition 2. Suppose $\mathbf{y} = \mathcal{A}(\rho) + \mathbf{v} + \mathbf{z}$ with the extended matrix $\mathcal{M} = [\mathcal{A}, I] \in \mathbb{C}^{m \times (d+m)}$. For $\delta \in [0, 1)$, if

$$m \geq C_2 r d \log^6 d, \quad \text{and} \quad \sup \|\mathbf{v}\|_\infty \leq \frac{\delta}{4\sqrt{ds}}, \quad (\text{A4})$$

for some constant $C_2 = O(1/\delta^2)$, then with high probability, \mathcal{M} has the GRIP constant satisfying $\delta_{r,s} \leq \delta$.

Proof. The GRIP constant $\delta_{r,s}$ can be equivalently expressed as

$$\delta_{r,s} = \sup_{(\rho, \mathbf{v}) \in \mathcal{T}} \left| \left\| \mathcal{M} \begin{bmatrix} \rho \\ \mathbf{v} \end{bmatrix} \right\|_2^2 - \|\rho\|_F^2 - \|\mathbf{v}\|_2^2 \right|, \quad (\text{A5})$$

where $\mathcal{T} := \{(\rho, \mathbf{v}): \text{rank}(\rho) \leq r, \|\mathbf{v}\|_0 \leq s, \|\rho\|_F^2 + \|\mathbf{v}\|_2^2 = 1, \rho \in \mathbb{C}^{d \times d}, \mathbf{v} \in \mathbb{R}^m\}$. With $\mathcal{M} = [\mathcal{A}, I]$, $\left\| \mathcal{M} \begin{bmatrix} \rho \\ \mathbf{v} \end{bmatrix} \right\|_2^2 = \|\mathcal{A}(\rho)\|_2^2 + \|\mathbf{v}\|_2^2 + 2\langle \mathcal{A}(\rho), \mathbf{v} \rangle$, the GRIP constant can be written as

$$\begin{aligned} \delta_{r,s} &= \sup_{(\rho, \mathbf{v}) \in \mathcal{T}} \left| \|\mathcal{A}(\rho)\|_2^2 + \|\mathbf{v}\|_2^2 + 2\langle \mathcal{A}(\rho), \mathbf{v} \rangle - \|\rho\|_F^2 - \|\mathbf{v}\|_2^2 \right| \\ &\leq \underbrace{\sup_{(\rho, \mathbf{v}) \in \mathcal{T}} \left| \|\mathcal{A}(\rho)\|_2^2 - \|\rho\|_F^2 \right|}_{\delta_1} + \underbrace{2 \sup_{(\rho, \mathbf{v}) \in \mathcal{T}} |\langle \mathcal{A}(\rho), \mathbf{v} \rangle|}_{\delta_2}. \end{aligned} \quad (\text{A6})$$

The aim is to derive a bound for the number of measurements m such that for any $\delta \in [0, 1)$, the GRIP constant $\delta_{r,s}$ is upper bounded by δ .

Recall the RIP definition as written in Eq. (2), we have

$$\delta_1 = \sup_{\rho \in \mathcal{D}_r} \left| \|\mathcal{A}(\rho)\|_2^2 - \|\rho\|_F^2 \right| \leq \delta. \quad (\text{A7})$$

Considering Theorem 2.1 of Ref. [40], we fix the constant $\delta \in [0, 1)$, and let $m = C \cdot r d \log^6 d$ for some constant $C = O(1/\delta^2)$ depending solely on δ . Then, over the choice of $\{P_1, \dots, P_m\}$, the map \mathcal{A} satisfies the RIP with high probability over the set of all $X \in \mathbb{C}^{d \times d}$ such that $\|X\|_{\text{tr}} \leq \sqrt{r}\|X\|_F$. Here, the set of all $X \in \mathbb{C}^{d \times d}$ with $\|X\|_{\text{tr}} \leq \sqrt{r}\|X\|_F$ is slightly larger than the set of all $X \in \mathbb{C}^{d \times d}$ with rank r . Furthermore, the failure probability is exponentially small in $\delta^2 C$. Then, for $\delta \in [0, 1)$, $m = 4Crd \log^6 d$ for some constant $C = O(1/\delta^2)$, $\delta_1 \leq \delta/2$ holds with high probability. Therefore, proof of the GRIP condition reduces to bounding the term δ_2 .

Now consider $\rho \succeq 0$, $\text{Tr}(\rho) = 1$, thus $\mathcal{A}(\rho)$ is a real vector,

$$\begin{aligned} \delta_2 &= 2 \sup_{(\rho, \mathbf{v}) \in \mathcal{T}_q} |\langle \mathcal{A}(\rho), \mathbf{v} \rangle| = 2 \sqrt{\frac{d}{m}} \sup_{(\rho, \mathbf{v}) \in \mathcal{T}_q} \left| \sum_{i=1}^m \text{Tr}(P_i \rho) v_i \right| \\ &= 2 \sqrt{\frac{d}{m}} \sup_{(\rho, \mathbf{v}) \in \mathcal{T}_q} |\langle \mathbf{u}, \mathbf{v} \rangle|, \end{aligned} \quad (\text{A8})$$

where $\mathbf{u} = \mathbf{u}(\rho) = (\text{Tr}(P_1 \rho), \text{Tr}(P_2 \rho), \dots, \text{Tr}(P_m \rho))^\top$, and $u_i = \text{Tr}(P_i \rho) \in [-1, 1]$; $\mathcal{T}_q = \{(\rho, \mathbf{v}): \rho \in \mathcal{X}, \mathbf{v} \in \mathcal{V}\}$, and $\mathcal{X} = \{\rho \in \mathbb{C}^{d \times d}: \rho \succeq 0, \text{Tr}(\rho) = 1, \text{rank}(\rho) \leq r\}$, $\mathcal{V} = \{\mathbf{v} \in \mathbb{R}^m: \|\mathbf{v}\|_0 \leq s\}$. Note that $\sup_{\rho \in \mathcal{X}} \|\mathbf{u}\|_2 = \sup_{\rho \in \mathcal{X}} \sqrt{\sum_{i=1}^m u_i^2} \leq \sqrt{\sum_{i=1}^m 1} = \sqrt{m}$, and

$$\sup_{\mathbf{v} \in \mathcal{V}} \|\mathbf{v}\|_2 = \sup_{\mathbf{v} \in \mathcal{V}} \sqrt{\sum_{i \in \text{supp}(\mathbf{v})} v_i^2} \leq \sqrt{s} \sup_{\mathbf{v} \in \mathcal{V}} \|\mathbf{v}\|_\infty, \quad (\text{A9})$$

where $\text{supp}(\mathbf{v}) := \{j \in \{1, \dots, m\} : v_j \neq 0\}$ denotes the set of indices corresponding to the nonzero entries of \mathbf{v} , and $\|\mathbf{v}\|_\infty = \max_i |v_i|$. From the Cauchy-Schwarz inequality, we can get

$$\begin{aligned} \sup_{(\rho, \mathbf{v}) \in \mathcal{T}_q} |\langle \mathbf{u}, \mathbf{v} \rangle| &\leq \sup_{\rho \in \mathcal{X}} \|\mathbf{u}\|_2 \cdot \sup_{\mathbf{v} \in \mathcal{V}} \|\mathbf{v}\|_2 \\ &\leq \sup \sqrt{ms} \|\mathbf{v}\|_\infty. \end{aligned} \quad (\text{A10})$$

Therefore,

$$\begin{aligned} \delta_2 &= 2 \sqrt{\frac{d}{m}} \sup_{(\rho, \mathbf{v}) \in \mathcal{T}_q} |\langle \mathbf{u}, \mathbf{v} \rangle| \\ &\leq \sup 2 \sqrt{ds} \|\mathbf{v}\|_\infty. \end{aligned} \quad (\text{A11})$$

To ensure $\delta_2 \leq \delta/2$, it suffices to impose

$$\sup \|\mathbf{v}\|_\infty \leq \frac{\delta}{4\sqrt{ds}}. \quad (\text{A12})$$

Combining $\delta_1 \leq \delta/2$ and $\delta_2 \leq \delta/2$, we get $\delta_{r,s} \leq \delta$, concluding the proof. \square

Remark 1. The GRIP condition can be used to prove the recovery guarantee. Note that the upper bound on the noise in Eq. (A4) may correspond to a worst-case scenario. The actual recovery error also depends on the choice of estimator and its associated reconstruction strategy. Furthermore, when analyzing the condition $\delta_2 \leq c\delta$, one can also obtain an alternative bound in a probabilistic sense by employing techniques such as covering numbers.

Appendix B: Process matrices of various quantum gates

In this section, we present explicit process-matrix representations of various quantum gates under the Pauli bases. In addition, the reconstruction results for the CZ and SWAP gates are shown in Fig. 8, while the reconstruction results for the Fredkin gate are presented in Fig. 9. These results serve as references for the numerical simulations and reconstructions discussed in the main text.

1. Two-qubit CNOT, CZ, and SWAP gates

The matrix form of two-qubit CNOT gate is represented as follows:

$$U_{\text{CNOT}} = \begin{bmatrix} 1 & 0 & 0 & 0 \\ 0 & 1 & 0 & 0 \\ 0 & 0 & 0 & 1 \\ 0 & 0 & 1 & 0 \end{bmatrix}. \quad (\text{B1})$$

Recall that the process matrix of a channel $\mathcal{E}(\rho) = \sum_i E_i \rho E_i^\dagger = \sum_{\alpha, \beta=1}^{d^2} \chi_{\alpha\beta} \Gamma_\alpha \rho \Gamma_\beta^\dagger$. The CNOT gate is unitary, so the corresponding channel $\mathcal{E}_{\text{CNOT}}(\rho) = U_{\text{CNOT}} \rho U_{\text{CNOT}}^\dagger$ has a single Kraus operator. Therefore, $U_{\text{CNOT}} = \sum_{\alpha=1}^{d^2} e_\alpha \Gamma_\alpha, \chi_{\alpha\beta} = e_\alpha e_\beta^*$.

Using Pauli bases representation, the CNOT gate can be written as $U_{\text{CNOT}} = \frac{1}{2}(I \otimes I + I \otimes X + Z \otimes I - Z \otimes X)$ of the tensor products of Pauli operators $\{I, X, Y, Z\}$ [3]. Consequently, the 16×16 process matrix has 16 non-zero elements, see Table I. Note that $\text{Tr}(\Gamma_\alpha^\dagger \Gamma_\beta) = d\delta_{\alpha\beta}$ if $\{\Gamma_\alpha \in \mathbb{C}^{d \times d}\}$ are the Pauli bases, for a trace-preserving operation $\text{Tr}(\chi^{\text{Pau}}) = 1$.

The form of the process matrix is dependent on the choice of bases. We also provide the representations in the computational and singular value decomposition (SVD) bases for reference. Using the computational bases representation, the CNOT can be written as $U_{\text{CNOT}} = |00\rangle\langle 00| + |01\rangle\langle 01| + |10\rangle\langle 11| + |11\rangle\langle 10|$. Consequently, the process matrix has 16 non-zero elements, see Table II. Note that $\text{Tr}(\Gamma_\alpha^\dagger \Gamma_\beta) = \delta_{\alpha\beta}$ if $\{\Gamma_\alpha \in \mathbb{C}^{d \times d}\}$ are the computational bases, for a trace-preserving operation $\text{Tr}(\chi^{\text{Com}}) = d$.

	<i>II</i>	<i>IX</i>	<i>ZI</i>	<i>ZX</i>	others
<i>II</i>	$\frac{1}{4}$	$\frac{1}{4}$	$\frac{1}{4}$	$-\frac{1}{4}$	0
<i>IX</i>	$\frac{1}{4}$	$\frac{1}{4}$	$\frac{1}{4}$	$-\frac{1}{4}$	0
<i>ZI</i>	$\frac{1}{4}$	$\frac{1}{4}$	$\frac{1}{4}$	$-\frac{1}{4}$	0
<i>ZX</i>	$-\frac{1}{4}$	$-\frac{1}{4}$	$-\frac{1}{4}$	$\frac{1}{4}$	0
others	0	0	0	0	0

TABLE I. Process matrix elements of the CNOT gate under Pauli bases. The order of bases is as follows: *II*, *IX*, *IY*, *IZ*, *XI*, *XX*, *XY*, *XZ*, *YI*, *YX*, *YY*, *YZ*, *ZI*, *ZX*, *ZY*, *ZZ*.

	$ 00\rangle\langle 00 $	$ 01\rangle\langle 01 $	$ 10\rangle\langle 11 $	$ 11\rangle\langle 10 $	others
$ 00\rangle\langle 00 $	1	1	1	1	0
$ 01\rangle\langle 01 $	1	1	1	1	0
$ 10\rangle\langle 11 $	1	1	1	1	0
$ 11\rangle\langle 10 $	1	1	1	1	0
others	0	0	0	0	0

TABLE II. Process matrix elements of the CNOT gate under the computational bases.

The representation under the SVD bases can be obtained through the following steps. First, perform SVD on the process matrix in the computational bases χ^{Com} :

$$\chi^{\text{Com}} = V \text{diag}(d, 0, \dots, 0) V^\dagger, \quad (\text{B2})$$

where V is a $d^2 \times d^2$ unitary matrix. Then, the SVD-bases matrices can be obtained by

$$\{\Gamma_\alpha^{\text{SVD}} = \sum_{\beta=1}^{d^2} V_{\beta\alpha} \Gamma_\beta^{\text{Com}} \in \mathbb{C}^{d \times d}\}_{\alpha=1}^{d^2}, \quad (\text{B3})$$

where $\Gamma_\beta^{\text{Com}} \in \mathbb{C}^{d \times d}$ is the computational bases. The CNOT can be represented as $U_{\text{CNOT}} = 2\Gamma_1^{\text{SVD}}$. Therefore, the process matrix has only one non-zero element $\chi_{11}^{\text{SVD}} = 4$. Note that $\text{Tr}(\Gamma_\alpha^\dagger \Gamma_\beta) = \delta_{\alpha\beta}$ if $\{\Gamma_\alpha \in \mathbb{C}^{d \times d}\}$ are the SVD bases, for a trace-preserving operation $\text{Tr}(\chi^{\text{SVD}}) = d$.

The matrix form of the CZ gate is represented as follows:

$$U_{\text{CZ}} = \begin{bmatrix} 1 & 0 & 0 & 0 \\ 0 & 1 & 0 & 0 \\ 0 & 0 & 1 & 0 \\ 0 & 0 & 0 & -1 \end{bmatrix}. \quad (\text{B4})$$

Using Pauli bases representation, the CZ gate can be written as $U_{\text{CZ}} = \frac{1}{2}(I \otimes I + I \otimes Z + Z \otimes I - Z \otimes Z)$ of the tensor products of Pauli operators $\{I, X, Y, Z\}$; see Table III.

The matrix form of the SWAP gate is represented as follows:

$$U_{\text{SWAP}} = \begin{bmatrix} 1 & 0 & 0 & 0 \\ 0 & 0 & 1 & 0 \\ 0 & 1 & 0 & 0 \\ 0 & 0 & 0 & 1 \end{bmatrix}. \quad (\text{B5})$$

Using Pauli bases representation, the SWAP gate can be written as $U_{\text{SWAP}} = \frac{1}{2}(I \otimes I + X \otimes X + Y \otimes Y + Z \otimes Z)$ of the tensor products of Pauli operators $\{I, X, Y, Z\}$; see Table IV.

The reconstruction results for the CZ and SWAP gates are shown in Fig. 8, while the results for the CNOT gate can be found in Fig. 5 in the main text.

	<i>II</i>	<i>IZ</i>	<i>ZI</i>	<i>ZZ</i>	others
<i>II</i>	$\frac{1}{4}$	$\frac{1}{4}$	$\frac{1}{4}$	$-\frac{1}{4}$	0
<i>IZ</i>	$\frac{1}{4}$	$\frac{1}{4}$	$\frac{1}{4}$	$-\frac{1}{4}$	0
<i>ZI</i>	$\frac{1}{4}$	$\frac{1}{4}$	$\frac{1}{4}$	$-\frac{1}{4}$	0
<i>ZZ</i>	$-\frac{1}{4}$	$-\frac{1}{4}$	$-\frac{1}{4}$	$\frac{1}{4}$	0
others	0	0	0	0	0

TABLE III. Process matrix elements of the CZ gate under Pauli bases. The order of bases is as follows: $II, IX, IY, IZ, XI, XX, XY, XZ, YI, YX, YY, YZ, ZI, ZX, ZY, ZZ$.

	<i>II</i>	<i>XX</i>	<i>YY</i>	<i>ZZ</i>	others
<i>II</i>	$\frac{1}{4}$	$\frac{1}{4}$	$\frac{1}{4}$	$\frac{1}{4}$	0
<i>XX</i>	$\frac{1}{4}$	$\frac{1}{4}$	$\frac{1}{4}$	$\frac{1}{4}$	0
<i>YY</i>	$\frac{1}{4}$	$\frac{1}{4}$	$\frac{1}{4}$	$\frac{1}{4}$	0
<i>ZZ</i>	$\frac{1}{4}$	$\frac{1}{4}$	$\frac{1}{4}$	$\frac{1}{4}$	0
others	0	0	0	0	0

TABLE IV. Process matrix elements of the SWAP gate under Pauli bases. The order of bases is as follows: $II, IX, IY, IZ, XI, XX, XY, XZ, YI, YX, YY, YZ, ZI, ZX, ZY, ZZ$.

2. Three-qubit Toffoli and Fredkin gates

The matrix form of three-qubit Toffoli gate is represented as follows:

Using Pauli bases representation, the Toffoli gate can be written as

$$U_{\text{Tof}} = \frac{1}{4} (3I \otimes I \otimes I + I \otimes I \otimes X + I \otimes Z \otimes I - I \otimes Z \otimes X + Z \otimes I \otimes I - Z \otimes I \otimes X - Z \otimes Z \otimes I + Z \otimes Z \otimes X) \quad (\text{B7})$$

of the tensor products of Pauli operators $\{I, X, Y, Z\}$; see Table V.

The matrix form of three-qubit Fredkin gate is given as

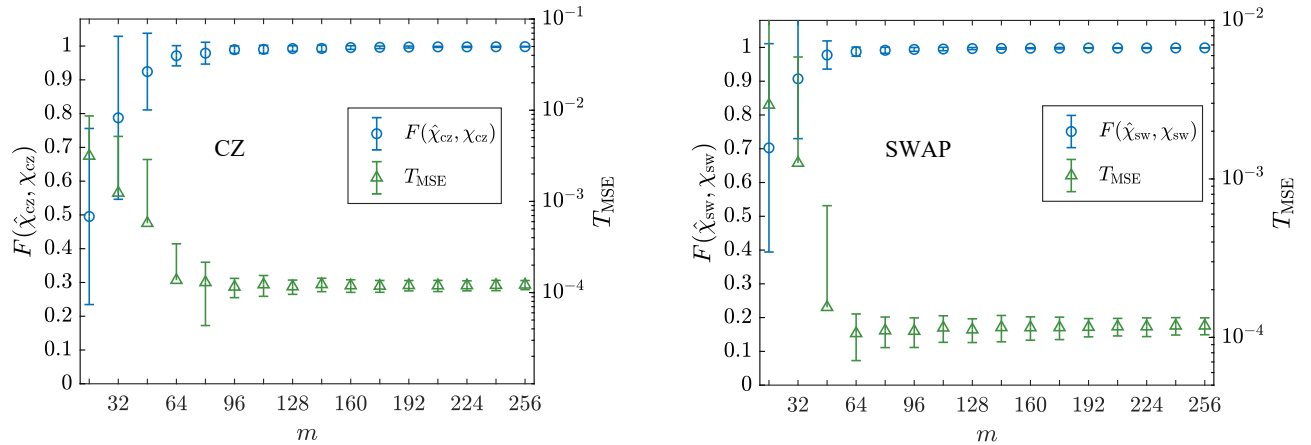


FIG. 8. Fidelity $F(\hat{\chi}, \chi)$ and MSE T_{MSE} as functions of the number of configurations m for the CZ and SWAP gates. The error bars are obtained from 100 runs of tomography, with each run selecting m combinations randomly. The blue points represent the fidelity between the reconstructed process matrix and true process matrix. The green points show the MSE between the reconstructed sparse Gaussian noise and true sparse Gaussian noise. The Gaussian noise has a mean of zero, a standard deviation of 1, and a sparsity level of $s = \lfloor 0.1m \rfloor$. The regularization parameters are chosen as $\mu_1 = 10^{-5}$, $\mu_2 = 10^{-3}$.

TABLE V. Process matrix elements of the Toffoli gate under Pauli bases. The order of the Pauli bases is as follows: $III, IIX, IIY, IIZ, \dots, ZZZ$.

Using Pauli bases representation, the Fredkin gate can be written as

$$U_{\text{Fred}} = \frac{1}{4}(3I \otimes I \otimes I + I \otimes X \otimes X + I \otimes Y \otimes Y + I \otimes Z \otimes Z + Z \otimes I \otimes I - Z \otimes X \otimes X - Z \otimes Y \otimes Y - Z \otimes Z \otimes Z) \quad (\text{B9})$$

of the tensor products of Pauli operators $\{I, X, Y, Z\}$; see Table VI. The reconstruction results for the Fredkin gate are shown in Fig. 9 as a supplementary illustration to the main text.

	<i>III</i>	<i>IIX</i>	<i>IYY</i>	<i>IIZ</i>	<i>ZII</i>	<i>ZXX</i>	<i>ZYY</i>	<i>ZZZ</i>	others
<i>III</i>	$\frac{9}{16}$	$\frac{3}{16}$	$\frac{3}{16}$	$\frac{3}{16}$	$\frac{3}{16}$	$-\frac{3}{16}$	$-\frac{3}{16}$	$-\frac{3}{16}$	0
<i>IIX</i>	$\frac{3}{16}$	$\frac{1}{16}$	$\frac{1}{16}$	$\frac{1}{16}$	$\frac{1}{16}$	$-\frac{1}{16}$	$-\frac{1}{16}$	$-\frac{1}{16}$	0
<i>IYY</i>	$\frac{3}{16}$	$\frac{1}{16}$	$\frac{1}{16}$	$\frac{1}{16}$	$\frac{1}{16}$	$-\frac{1}{16}$	$-\frac{1}{16}$	$-\frac{1}{16}$	0
<i>IIZ</i>	$\frac{3}{16}$	$\frac{1}{16}$	$\frac{1}{16}$	$\frac{1}{16}$	$\frac{1}{16}$	$-\frac{1}{16}$	$-\frac{1}{16}$	$-\frac{1}{16}$	0
<i>ZII</i>	$\frac{3}{16}$	$\frac{1}{16}$	$\frac{1}{16}$	$\frac{1}{16}$	$\frac{1}{16}$	$-\frac{1}{16}$	$-\frac{1}{16}$	$-\frac{1}{16}$	0
<i>ZXX</i>	$-\frac{3}{16}$	$-\frac{1}{16}$	$-\frac{1}{16}$	$-\frac{1}{16}$	$-\frac{1}{16}$	$\frac{1}{16}$	$\frac{1}{16}$	$\frac{1}{16}$	0
<i>ZYY</i>	$-\frac{3}{16}$	$-\frac{1}{16}$	$-\frac{1}{16}$	$-\frac{1}{16}$	$-\frac{1}{16}$	$\frac{1}{16}$	$\frac{1}{16}$	$\frac{1}{16}$	0
<i>ZZZ</i>	$-\frac{3}{16}$	$-\frac{1}{16}$	$-\frac{1}{16}$	$-\frac{1}{16}$	$-\frac{1}{16}$	$\frac{1}{16}$	$\frac{1}{16}$	$\frac{1}{16}$	0
others	0	0	0	0	0	0	0	0	0

TABLE VI. Process matrix elements of the Fredkin gate under Pauli bases. The order of the Pauli bases is as follows: *III*, *IIX*, *IYY*, *IIZ*, ..., *ZZZ*.

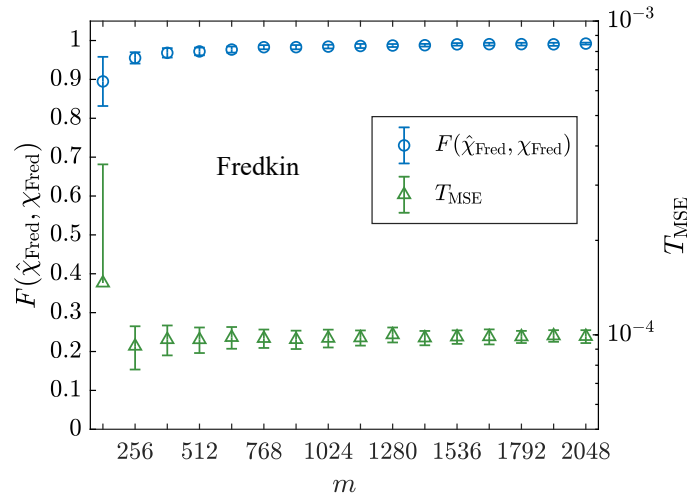


FIG. 9. Fidelity $F(\hat{\chi}_{\text{Fred}}, \chi_{\text{Fred}})$ and MSE T_{MSE} as functions of the number of configurations m . The error bars are obtained from 50 runs of tomography, with each run selecting m combinations randomly. The blue points represent the fidelity between the reconstructed process matrix and true process matrix of the Fredkin gate. The green points show the MSE between the reconstructed sparse Gaussian noise and true sparse Gaussian noise. The Gaussian noise has a mean of zero, a standard deviation of 1, and a sparsity level of $s = \lfloor 0.1m \rfloor$. The regularization parameters are chosen as $\mu_1 = 10^{-5}$, $\mu_2 = 10^{-3}$.

3. Four-qubit CCCZ gate

Using Pauli bases representation, the CCCZ gate can be written as

$$\begin{aligned}
 U_{\text{CC CZ}} = & \frac{1}{8} (7\text{III}I + \text{IIIZ} + \text{IIZI} - \text{IIZZ} \\
 & + \text{IZII} - \text{IZIZ} - \text{IZZI} + \text{IZZZ} \\
 & + \text{ZIII} - \text{ZIIZ} - \text{ZIZI} + \text{ZIZZ} \\
 & - \text{ZZII} + \text{ZZIZ} + \text{ZZZI} - \text{ZZZZ}).
 \end{aligned} \tag{B10}$$

See Table VII for the process matrix elements of the CCCZ gate under Pauli bases.

TABLE VII. Process matrix elements of the CCCZ gate under Pauli bases. The order of the Pauli bases is as follows: III , III X , II Y , II Z , ..., ZZZ .